Statistical Downscaling of Daily Wind Speed Variations

MEGAN C. KIRCHMEIER

Department of Atmospheric and Oceanic Sciences and Center for Climatic Research, University of Wisconsin—Madison, Madison, Wisconsin

DAVID J. LORENZ

Center for Climatic Research, University of Wisconsin—Madison, Madison, Wisconsin

DANIEL J. VIMONT

Department of Atmospheric and Oceanic Sciences and Center for Climatic Research, University of Wisconsin—Madison, Madison, Wisconsin

(Manuscript received 10 July 2013, in final form 6 December 2013)

ABSTRACT

This study presents the development of a method to statistically downscale daily wind speed variations in an extended Great Lakes region. A probabilistic approach is used, predicting a daily-varying probability density function (PDF) of local-scale daily wind speed conditioned on large-scale daily wind speed predictors. Advantages of a probabilistic method are that it provides realistic information on the variance and extremes in addition to information on the mean, it allows the autocorrelation of downscaled realizations to be tuned to match the autocorrelation of local-scale observations, and it allows flexibility in the use of the final downscaled product. Much attention is given to fitting the proper functional form of the PDF by investigating the observed local-scale wind speed distribution (predictand) as a function of the decile of the large-scale wind (predictor). It is found that the local-scale standard deviation and the local-scale shape parameter (from a gamma distribution) are nonconstant functions of the large-scale predictor. As such, a vector generalized linear model is developed to relate the large-scale and local-scale wind speeds. Maximum likelihood and cross validation are used to fit local-scale gamma distribution shape and scale parameters to the large-scale wind speed. The result is a daily-varying probability distribution of local-scale wind speed, conditioned on the large-scale wind speed.

1. Introduction

Downscaling allows high-resolution information to be extracted from large-scale models, particularly under future scenarios for which no observational data are available. There are two main classes of downscaling: statistical and dynamical. Dynamical downscaling typically employs the use of a regional climate model (RCM) embedded within, or driven by output from, a larger-scale global model. Giorgi (2006) presents a more complete description of RCMs and dynamical downscaling. Although computationally expensive, dynamical downscaling often performs well in regions of complex terrain (Horvath et al. 2012) and produces local-scale values that are generally consistent with the large scale. Despite the advantage that models are physically based, it is also important to note that each regional model has its own sources of error.

Statistical downscaling involves developing a relationship between the large and local scales using historical data and then applying this relationship to adjust independent large-scale data down to the local scale. We define the local scale as point-station observations and the large scale as a coarse gridded dataset such as reanalyses or general circulation models. Use of this method relies on the assumption that the derived relationship between large- and local-scale data remains stationary when applied to new large-scale data (e.g., future model scenarios, independent time periods, or independent spatial locations). Few studies (e.g., Frías et al. 2006; Schmith 2008) have attempted to verify the stationarity of downscaling methods, but it is an important concept

Corresponding author address: Megan Kirchmeier, 1225 W. Dayton St., Madison, WI 53706.
E-mail: kirchmeier@wisc.edu

DOI: 10.1175/JAMC-D-13-0230.1

to consider before using any downscaled results. Statistical downscaling produces relatively low computational costs and is very flexible, not just in that the methods can be applied easily to several different global models (e.g., Najac et al. 2011) but also in that a variety of different information can be extracted (Michelangeli et al. 2009). An additional advantage is that statistical downscaling often adjusts for bias when applied to output from global climate models (e.g., Pryor et al. 2005). Statistical downscaling is limited by the availability of observations with which to develop the model. Deterministic statistical downscaling methods, which produce a single estimate of the predictand variable for each time step, often underestimate the variance and interannual variability (e.g., Schmidli et al. 2007; Bürger et al. 2012). A probabilistic downscaling approach, like the one we employ, produces a probability density function (PDF) for every time step and, in doing so, maintains information on the variance.

Statistical and dynamical downscaling methods can also be combined. Statistical downscaling methods can be used to downscale output from an RCM further or to correct biases from dynamical downscaling (e.g., Oh et al. 2004; Leander and Buishand 2007; Engen-Skaugen 2007). Often these methods use a model output statistics (MOS) approach; Maraun et al. (2010b) present a more thorough description of the use of MOS downscaling methods for precipitation. In addition, an RCM can be run once for each weather type (e.g., Fuentes and Heimann 2000; Najac et al. 2011) or principal component (e.g., Martinez et al. 2013) to construct a local-scale time series that is based on frequency of occurrence.

The majority of downscaling studies focus on temperature and/or precipitation. Although most downscaling is done spatially (e.g., from 2° grid boxes to 0.1° grid boxes), the methods can also be applied temporally (e.g., from daily to hourly; Cheng et al. 2008). For a comprehensive overview of downscaling methods for precipitation, see Maraun et al. (2010b). For our purposes, it is important to highlight some studies using generalized linear models (GLM; McCullagh and Nelder 1989) or vector generalized linear models (VGLM; Yee and Stephenson 2007). GLMs predict a single distribution parameter whereas VGLMs predict a collection of distribution parameters. Yang et al. (2005) used a GLM to represent daily rainfall across multiple station locations. To investigate extreme events, Maraun et al. (2010a) used a VGLM to estimate the three parameters of the generalized extreme value (GEV) distribution for daily precipitation. Fealy and Sweeney (2007) used a GLM with the gamma distribution to downscale daily precipitation amount. Furthermore, generalized additive models (GAM; Hastie and Tibshirani 1986) are similar to GLMs but instead use a sum of nonparametric functions of the predictors. GAMs and their vectorized counterparts are also used for statistical downscaling. Vrac et al. (2007) developed a GAM to downscale temperature and precipitation over Europe and applied their methods to large-scale paleoclimatic data. Beckmann and Adri Buishand (2002) use a GAM to model the wet-day rainfall amounts at several stations on the basis of large-scale predictors.

While not as numerous as those for temperature and precipitation, there have been several studies that downscale wind. A wide range of wind variables have been predicted, including wind speed (e.g., de Rooy and Kok 2004), zonal u and meridional v components (e.g., Salameh et al. 2009; Monahan 2012), wind gusts (e.g., Cheng et al. 2012), maximum wind speed (e.g., Yan et al. 2002), and energy density (e.g., Pryor et al. 2005) on time scales from subdaily (e.g., de Rooy and Kok 2004) to daily (e.g., Yan et al. 2002) to monthly (e.g., Pryor et al. 2005; Monahan 2012).

In addition to dynamical or combination methods (e.g., Horvath et al. 2012; Najac et al. 2011; Mengelkamp et al. 1997), a variety of statistical methods have been developed and used for downscaling wind. Michelangeli et al. (2009) used a cumulative distribution function (CDF)–based approach, and Salameh et al. (2009) defined a GAM that established the u and v components as sums of spline functions. Pryor et al. (2005) focused on downscaling a Weibull PDF using a regression-based approach with relative vorticity and mean sea level pressure gradients as the large-scale predictors. De Rooy and Kok (2004) brought model wind speed down to 10 m using a local roughness length before applying linear regression. To assess extremes in wind speed, Yan et al. (2002) used a GLM with the gamma distribution to predict the daily maximum wind speed. Yan et al. (2002) considered numerous predictors, including seasonality, autocorrelation, and climate indices (the Arctic Oscillation, the North Atlantic Oscillation, etc.). On a monthly time scale, and downscaling over the ocean, Monahan (2012) had more success predicting the u and v components of the wind than predicting the wind speed or the standard deviation. Monahan (2012) also showed that downscaling to daily values and then averaging to a monthly scale has more skill than downscaling directly to monthly values. Van der Kamp et al. (2012) also produced better results predicting wind components as opposed to wind speed and found that predictability was better for components that were oriented along the topography. To investigate sea surface winds in the interest of upwelling, Goubanova et al. (2010) used multiple linear regression with gridded satellite-derived surface wind as the local-scale predictand.

This study presents a method for statistically downscaling a daily wind speed PDF. The model is adapted from a VGLM that allows both the gamma distribution shape and scale parameters of the local wind speed to vary as functions of the large-scale wind speed (large and local scales will be defined below). The result is a daily-varying probability distribution of local-scale wind speed conditioned on the large-scale wind speed for that day. Downscaling to a PDF rather than a specific value recognizes that, although there is shared information between the large and local scales, the local-scale wind speed is not exactly determined by the large-scale conditions on a given day. Instead, there is a range of possible local-scale wind speeds that may be observed for a given large-scale wind. The PDF is an attempt to quantify that range.

This paper is organized as follows. Section 2 contains a description of the large- and local-scale data. In section 3, the relationship between large- and local-scale daily wind speeds is explored. Section 4 describes the development of the statistical model. In section 5, examples of the downscaling output are shown and the performance of this downscaling method is evaluated.

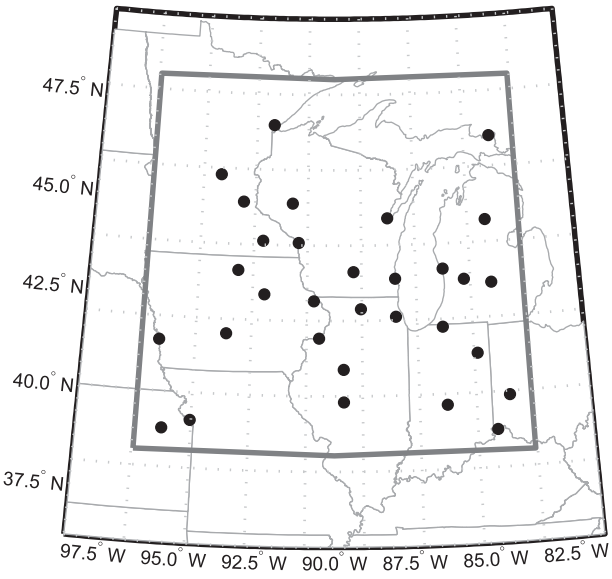

FIG. 1. A map of the 31 NWS first-order station locations used as the local scale. The dotted lines represent the reanalysis grid, and the dark-gray inner box displays the domain in which the first-order stations were chosen.

2. Data

a. Local scale

Local-scale data were obtained from the National Climatic Data Center (NCDC) Summary of the Day—First Order (Dataset 3210). Thirty-one National Weather Service (NWS) first-order stations were chosen in an extended western Great Lakes region, shown in Fig. 1. Station details are listed in Table 1. Daily average 10-m wind speed was acquired from each of these stations for the period of 1984–2010, chosen based on data availability. Only sites with full records (i.e., missing no more than 5% of all possible days and missing no more than 6 months of data each year) of wind data over this period were selected. See Table 1 for the length of each station's record.

Data were quality controlled with the following method. First, all days reporting a daily average wind speed of $0\,\mathrm{m\,s^{-1}}$ were removed (totaling 24 days across all sites). Additional suspect observations were flagged if the difference between the observed value and that from the reanalysis in the station-containing large-scale grid box was an outlier (z score > 3) and the observed value was greater than $3\,\mathrm{m\,s^{-1}}$ different from all three of its closest neighboring stations. Of all days at all sites (303 592 days), only 116 observations were flagged (across all sites), and these suspect observations were manually assessed; 46 were deemed bad on the basis of the manual inspection and were removed. The remaining observations were allowed to pass; these often occurred at sites along the Great Lakes that experience local topographical influences and that have a farther distance to their nearest neighbors.

Small changes in site location, corresponding to relocation within the airport, were identified at all stations through NCDC metadata. These changes in location were often accompanied by inhomogeneities in the wind speed record. The influence of these inhomogeneities is evident in the unrealistically high persistence in the autocorrelation functions (Fig. 2a). Note that for Madison, Wisconsin (MSN), the autocorrelation remains above 0.1 at lags out to 20 days and beyond, which suggests problems with the original data. To adjust for the inhomogeneities, a CDF-mapping approach was used (Panofsky and Brier 1958; Wood 2002). At each site, the time series was divided into sections on the basis of the station location and each section was adjusted by quantile matching to the longest section of data. First, 200 quantile values were determined for each portion of the time series. Next, for a certain portion to be adjusted, the difference between that portion's and the longest portion's wind speed values at each quantile was calculated. These differences were used as offsets. Then, for each day in that portion's time series, the quantile of its wind speed value was determined and the corresponding offset was applied. Since offsets were only calculated for 200 quantiles, weighted averaging was used when a day's quantile fell between those that were available. For the

TABLE 1. NWS first-order stations representing the local scale. Here, ID indicates the identifier label for the site.

Site ID	Location	State	Lat (°N)	Lon (°E)	No. of days*
DMX	Des Moines	IA	41.53	−93.66	9849
DBQ	Dubuque	IA	42.40	−90.70	9846
MCW	Mason City	IA	43.15	−93.33	9517
ALO	Waterloo	IA	42.55	−92.40	9844
ORD	Chicago O'Hare International Airport	IL	41.99	−87.91	9846
MLI	Moline	IL	41.46	−90.51	9839
PIA	Peoria	IL	40.67	−89.68	9854
RFD	Rockford	IL	42.20	−89.10	9854
SPI	Springfield	IL	39.85	−89.68	9846
FWA	Fort Wayne	IN	41.00	−85.20	9855
IND	Indianapolis	IN	39.72	−86.28	9853
SBN	South Bend	IN	41.70	−86.32	9851
TOP	Topeka	KS	39.07	−95.63	9773
CVG	Covington	KY	39.05	−84.67	9825
GRR	Gerald R. Ford International Airport (Grand Rapids)	MI	42.89	−85.53	9741
HTL	Houghton Lake, Roscommon County	MI	44.36	−84.68	9841
LAN	Lansing	MI	42.77	−84.59	9847
MKG	Muskegon	MI	43.17	−86.24	9849
ANJ	Sault Ste. Marie	MI	46.47	−84.35	9849
DLH	Duluth	MN	46.84	−92.20	9832
MSP	Minneapolis–St. Paul	MN	44.88	−93.22	9854
RST	Rochester	MN	43.91	−92.50	9849
STC	St. Cloud	MN	45.55	−94.06	9833
MCI	Kansas City International Airport	MO	39.31	−94.72	9848
OMA	Omaha	NE	41.31	−95.90	9640
DAY	Dayton	OH	39.90	−84.21	9851
EAU	Eau Claire	WI	44.87	−91.48	9420
GRB	Green Bay	WI	44.49	−88.13	9840
LSE	La Crosse	WI	43.87	−91.25	9391
MSN	Madison	WI	43.14	−89.34	9802
MKE	Milwaukee	WI	42.95	−87.90	9853

* Total number of days in the period is 9862.

lower tail, a check was applied to ensure that all wind speed values remained positive. For the upper tail (top 1%), linear regression was used to determine the offset, since a wide spread of wind speed values fell in this upper tail range.

An example is shown in Fig. 2c for MSN. The original time series (shown in gray) was divided into three sections on the basis of the dates of the station relocations (shown by vertical lines). The latter two sections were each adjusted to match the earliest and longest section. The time series after the adjustment process is shown in black. Relative to the prior autocorrelation functions, the autocorrelation functions after adjusting for inhomogeneities show less persistence (Fig. 2b). Adjusting for inhomogeneities at each site had little influence on the results of the downscaling method that we present here.

b. Large scale

To represent the large scale, National Centers for Environmental Prediction–National Center for Atmospheric Research four-times-daily reanalysis data (Kalnay et al. 1996) were acquired for the same date range of 1984–2010. First, four-times-daily wind speed magnitudes were calculated from the surface u and v components. Then, to match station observations determined from midnight to midnight central standard time (UTC − 6 h), four instantaneous wind speed magnitudes (0600, 1200, 1800, and 0000 UTC) were averaged to produce the daily wind speed from the large scale. Although some of the stations reported data in eastern standard time (UTC − 5 h), we were limited to the four-times-daily data and suspect a 1-h offset will have minimal influence.

One method used to create a large-scale time series for each station is to interpolate the gridded reanalysis data to the station's latitude–longitude point. For the final downscaling, another method based on correlation maps was found to perform better; this method will be discussed in more detail in later sections. With either method, the length of the time series was adjusted to match that of the station (i.e., days missing in observations were also removed from the reanalysis).

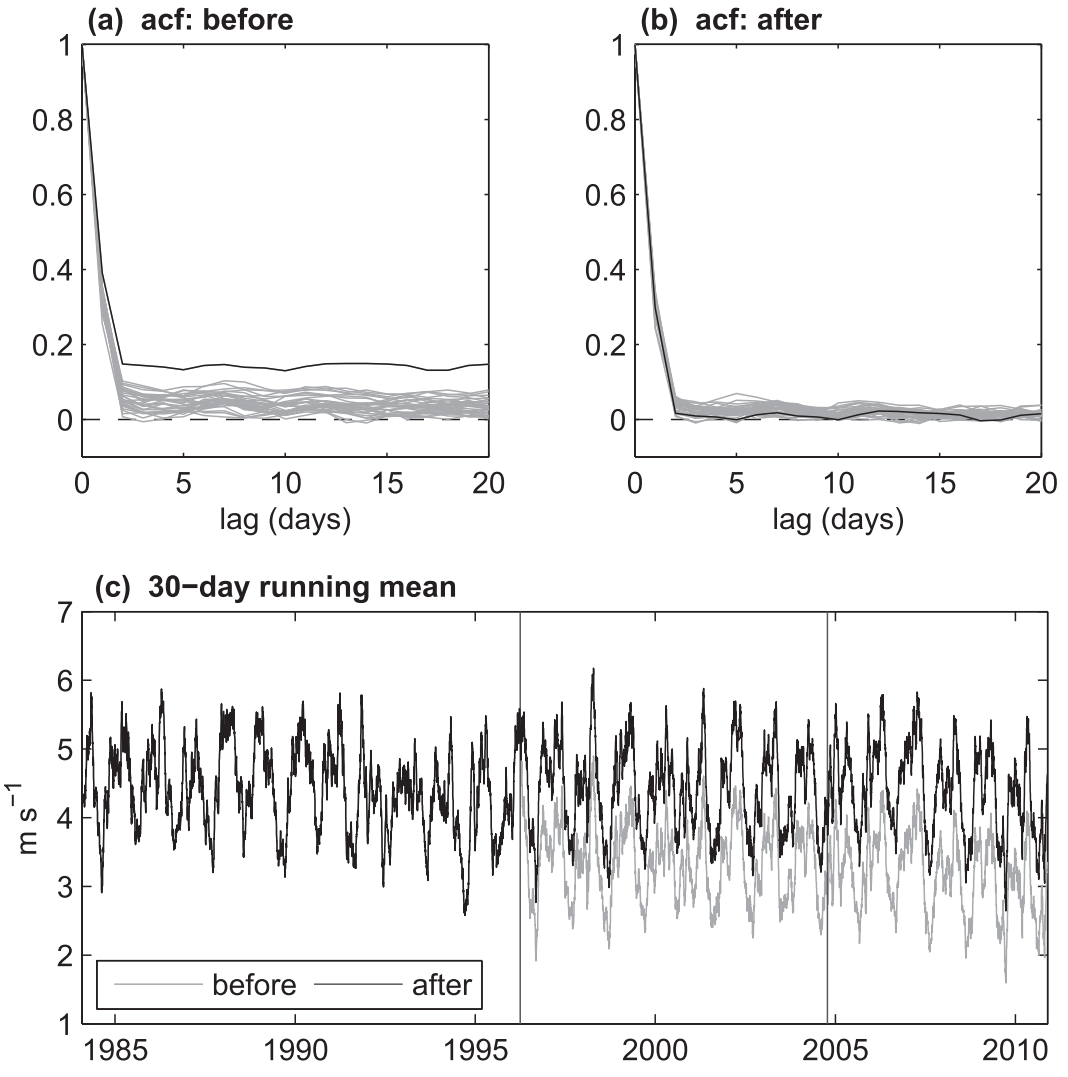

FIG. 2. Autocorrelation function (acf) for MSN (black line) and all other sites (gray lines) (a) before and (b) after adjusting for inhomogeneities. (c) The 30-day running mean for MSN before (gray line) and after (black line) adjusting for the inhomogeneities. Vertical lines indicate relocation dates.

3. Relationship between the large and local scales

In this section, we describe the relationship between the large-scale and local-scale wind variations, with the intent of identifying a statistical method that will best simulate this relationship. We first examine the structure of the bivariate PDF between the large-scale and local-scale winds and show that the assumptions underlying standard linear models (e.g., linear regression) are violated. Next, a month-by-month analysis is used to show that a seasonal model will be necessary. Third, we investigate three parametric PDFs to determine which best fits the data.

Estimates of the bivariate probability density between the large-scale and local-scale winds are shown in Fig. 3. Here, the large-scale time series for each station was determined using a linear interpolation of the gridded dataset to the station's location. The bivariate densities for January (Fig. 3a) and July (Fig. 3b) were determined using a bivariate Gaussian kernel density estimator; the contour intervals are nonlinear (and different between months) to highlight the important features. For January, although the dominant shape is linear, at wind speeds larger than about $7\,\mathrm{m\,s^{-1}}$ the PDF shows curvature toward larger local-scale wind speeds. This curvature shows a wider range of local-scale values given a certain large-scale value at the upper tail of the distribution than would be expected from a linear bivariate density. For July, similar curvature is evident at wind speeds larger than $5\,\mathrm{m\,s^{-1}}$. The dominant shape of the bivariate density is

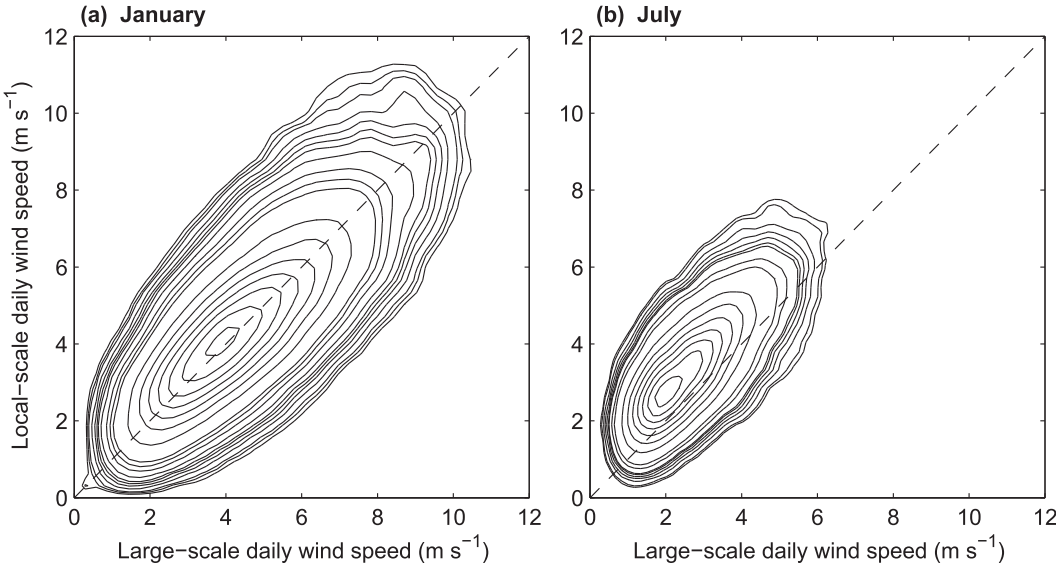

FIG. 3. Bivariate density between the large- and local-scale daily wind speeds from all stations for (a) January and (b) July. Note that the contour interval is nonlinear and is different for each month. The dashed line represents the one-to-one line.

still linear, but the structure deviates more from the dashed $y = x$ line than it did for January.

The discrepancy at high wind speeds was examined in more detail by plotting, in Fig. 4, the mean and standard deviation of the local-scale wind speed, conditional upon the decile of large-scale wind speed. Figure 4 was constructed by first separating the large-scale wind speed at each station into the deciles of its distribution and identifying the dates of the large-scale observations that fell in each bin. For the dates in each decile bin, the local-scale mean and standard deviation were calculated for each location. Figure 4 shows the mean (Figs. 4a,c) and standard deviation (Figs. 4b,d) values for individual stations in gray and for the average across all stations in black. For plotting purposes, the local-scale composites for each station (gray curves) and for all stations (black) are plotted against the mean of the large-scale wind across all stations for each decile. Methods such as linear regression or a GLM for relating the large-scale winds to the local-scale winds require the conditional means to be roughly linear and/or the conditional standard deviations to be constant. In this case, the conditional means are roughly linear. The conditional standard deviations are not constant, however, especially at higher large-scale wind speeds, confirming the results from the bivariate distribution in Fig. 3. As such, a standard linear regression model would underestimate the local-scale wind variations during periods of high large-scale wind speed. These results motivate the use and structure of the VGLM, as described in section 4.

Despite the inability of linear regression to represent adequately the full relationship between the large- and local-scale winds, Figs. 4a,c suggest that the conditional means are approximately linearly related. As such, linear regression can be used to examine the influence of seasonality on the relationship between the large- and local-scale wind speeds. Figure 5 displays the regression slopes by month for individual stations in gray and for the average across all sites in black. The regression of large-scale daily wind speed onto local-scale daily wind speed produces slope parameters that vary depending on the month. As a result, using the entire dataset (the asterisks in Fig. 5) will not capture the relationship between large- and local-scale wind as accurately as dividing the data by month. Hence, any further analysis will be implemented for each month separately.

To choose a distribution on which to base the statistical model, three different distributions (normal, gamma, and Weibull) were fit to the local-scale wind speeds, conditional upon the large-scale decile. As with Fig. 4, the local-scale observations were binned according to their same date's large-scale decile and then the given distributions were fit to the values in each bin. The resulting negative log-likelihood $[-\log(L)]$ values were summed across all sites. Because the maximum likelihood is desired, the distribution with the smallest $-\log(L)$ values will be optimal. Although the differences are small (generally $< 6\%$), both the gamma and normal distributions consistently produced better $-\log(L)$ values than did the Weibull distribution. The gamma distribution also

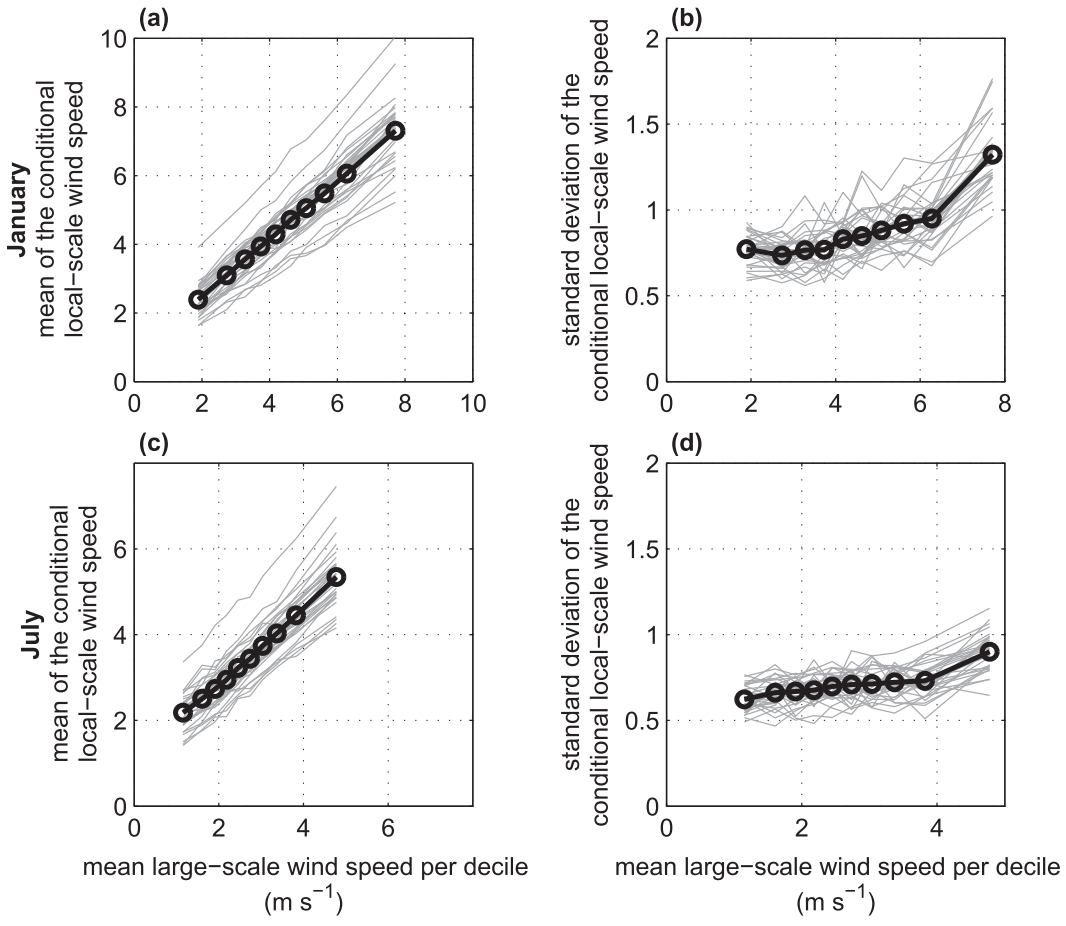

FIG. 4. (left) Mean and (right) standard deviation of the local-scale wind speed for the months of (a),(b) January and (c),(d) July, conditional upon the decile of the large-scale wind speed. Gray lines represent individual stations, and the solid black line shows the mean across all stations.

has the benefit of a forced cutoff at zero, which is necessary for wind speed. As a result, the gamma distribution was chosen for the downscaling model.

The PDF of the gamma distribution with shape parameter a and scale parameter b is

$$f(y) = \frac{b^{-a}}{\Gamma(a)} y^{a-1} \exp\left(-\frac{y}{b}\right). \quad (1)$$

The shape parameter of this gamma distribution fit for the local-scale wind, conditional upon the decile of large-scale wind speed is plotted in Fig. 6 for both January (Fig. 6a) and July (Fig. 6b). Again, individual sites are shown in gray, and the average across all sites is in black. The shape parameter varies greatly as a function of large-scale wind speed; hence, a GLM, which requires a constant shape parameter, would be too restrictive. In addition, individual sites show more noise with the gamma-distribution shape parameter when compared with the mean and standard deviation from Fig. 4.

To summarize, the mean of the local-scale daily wind speed is approximately linearly related to the mean of the large-scale daily wind speed, and the standard deviation of the local-scale daily wind speed is not constant with respect to the mean of the large-scale daily wind speed. In addition, the relationship between the large- and local-scale wind speeds varies seasonally. Last, the gamma distribution best fits the local-scale data and has additional desirable properties, although its shape parameter varies with the mean of the large-scale wind speed. These relationships motivate our choice of model for the downscaling routine.

4. Development of the statistical model

In this section, we describe the development of the statistical model that characterizes the relationship between the large- and local-scale daily wind speeds. First, we discuss our choice of model, which is adapted from the framework of a VGLM. Next, we consider the large-scale

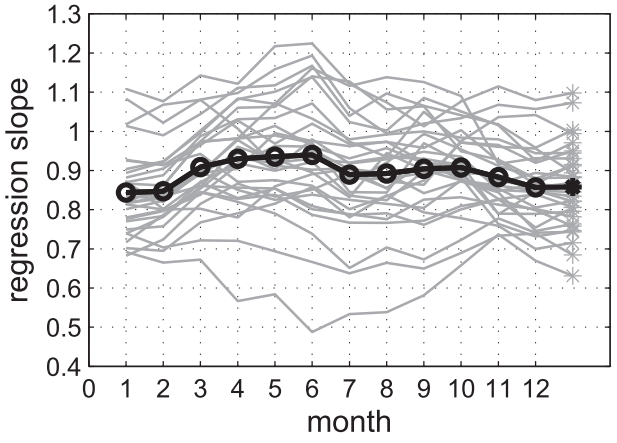

FIG. 5. Slopes from a simple linear regression, using the large scale to predict the local-scale daily wind speed. Individual sites are shown in gray; the average across all sites is shown in black. Asterisks represent the slope if using the entire year.

predictors, including both the formation of the large-scale time series and the choice of model predictors.

a. Choice of model

To set up our method, it is helpful to discuss the framework of a GLM. [For more information, see McCullagh and Nelder (1989).] For a GLM, the terminology involves predicting the distribution of y as a function of $\mathbf{x}$, where the expected value of y is the mean μ. In addition, $\eta = \mathbf{x}\boldsymbol{\beta}$, where $\mathbf{x}$ is the predictors and $\boldsymbol{\beta}$ is a vector of model parameters (or regression coefficients). A link function g is chosen such that $\mu = g^{-1}(\eta)$. Linear regression is the simplest case of a GLM, utilizing the normal distribution with an identity link function where $\mu = \eta$. The definition of a GLM link function allows only a single value for the shape parameter of a distribution, since this characterization of the distribution must remain constant; the location or scale parameter is allowed to vary, however.

Our goal is to predict features of the local-scale daily wind speed y as a function of the large-scale daily wind speed x. The model, and thus x and y, are defined separately for each site and for each month. Instead of predicting a single value for the wind speed for each day, we will predict the distribution of possible daily wind speed values for each day. We accomplish this by defining a vector model to estimate the two parameters of the gamma distribution describing each day's daily wind speed, conditioned on the large-scale wind speed for that day. Although a GLM is a good place to start, this model's structure allows the scale parameter to vary while holding the shape parameter constant. Figure 6 shows that this attribute is unacceptable. Thus, to let the shape parameter vary as well, we must adapt the structure of a GLM and base our model on a VGLM instead.

We found a better, more stable fit for the mean and standard deviation of the local scale as functions of the large-scale wind, as opposed to using the scale and shape parameters as functions of the large-scale wind. Evidence for this improvement is suggested by comparing Figs. 4 and 6. For individual sites, there is more variability in the shape parameter; the same is also true for the scale parameter (not shown). A key advantage of the gamma distribution is that the mean μ and standard deviation σ are related to the shape parameter a and scale parameter b through simple functions:

$$\mu = ab \quad \text{and} \quad \sigma = a^{1/2}b. \tag{2}$$

Thus, it is a simple switch to use the mean and standard deviation instead of the scale and shape parameters. As

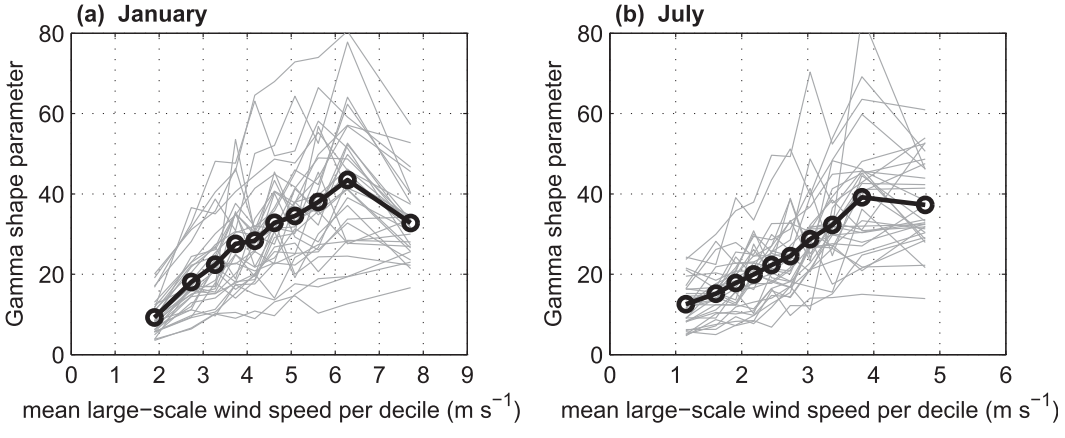

FIG. 6. Shape parameter of the gamma distribution fit for the local-scale daily wind speed, conditional upon the decile of that day's large-scale wind speed, for (a) January and (b) July. Individual sites are shown in gray, and the average across all sites is shown in black.

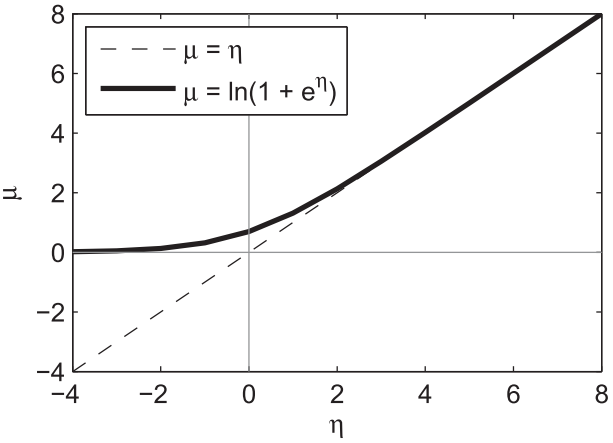

FIG. 7. Link functions $\mu = g^{-1}(\eta)$.

such, the mean and standard deviation were each defined as functions of the large-scale wind speed with three parameters through a quasi-linear link function and following the framework of a VGLM:

$$\mu = g_\mu^{-1}(\eta_\mu) = \alpha_\mu \ln[1 + \exp(\eta_\mu/\alpha_\mu)] \quad \text{and} \qquad (3)$$

$$\sigma = g_\sigma^{-1}(\eta_\sigma) = \alpha_\sigma \ln[1 + \exp(\eta_\sigma/\alpha_\sigma)], \qquad (4)$$

where $\eta_\mu = \gamma_0 + \gamma_1 x + \gamma_2 x^2$ and $\eta_\sigma = D_0 + D_1 x + D_2 x^2$. Here, x represents the large-scale wind speed for the given site and month, the γ and D values are coefficients determining the influence of each predictor, and α_μ and α_σ are coefficients in the link function defined across all sites and months. The x^2 term, the square of the large-scale wind speed, was added on the basis of the curvature in the standard deviation relationship shown in Fig. 4. In addition, x^2 was also used in the equation for μ to account for any slight curvature within the individual sites. This link function,

$$g^{-1}(\eta) = \alpha \ln[1 + \exp(\eta/\alpha)],$$

was chosen to maintain a mostly linear relationship between the large-scale predictors and the mean and standard deviation but to keep the values of the mean and standard deviation greater than 0. Figure 7 shows a comparison between the link function chosen (with $\alpha = 1$) and the identity link $\mu = \eta$. The link-function coefficients $\alpha_\mu = 0.75$ and $\alpha_\sigma = 0.25$ were chosen to minimize the $-\log(L)$ values from the model fit across all sites and months.

After defining the PDF of the gamma distribution in terms of the mean and standard deviation, the appropriate functions (μ and σ above) were inserted and a likelihood function was derived. Matlab (proprietary software) optimization routines were used to find the values of the six coefficients (γ_0, γ_1, γ_2, D_0, D_1, and D_2) that maximized the likelihood for each site and month. A derivative-free, simplex search algorithm (Lagarias et al. 1998) was chosen because of its consistency of converging. This routine was chosen over the constrained derivative-based "trust region" method (Coleman and Li 1996). When both methods reached a solution (about 80% of the time), the coefficient values chosen were very similar. Additional motivation for the link function shown above, instead of the identity link, is that it helped these routines to converge on a solution.

b. Choice of predictors

Since our downscaling method was designed to be used pointwise (i.e., separately for each of the local-scale observing stations), a single large-scale time series is needed for each station point. This large-scale time series serves as x in the predictors presented above. There are several methods for determining a point time series from a gridded dataset. The first is to use the values from the station-containing grid box. Problems may arise with stations located near gridbox boundaries, however. The second method is to interpolate from the grid to the single point. The third is to use empirically derived weights to construct a weighted average over all grid boxes to represent the point. We used the correlation map for the empirically derived weights.

Figure 8 displays the correlation between a site (MSN) and each grid box of the reanalysis for both January (Fig. 8a) and July (Fig. 8c). In general, the higher correlations are spread over a greater distance during the winter than during the summer. As an alternative to interpolating to the station's point, the correlations can be used as weights for each grid point to build the large-scale time series. First, the correlation map was raised to a large, odd power to focus the spatial influence. Because of the seasonality of the correlation maps, the power was chosen separately for each month on the basis of maximizing the explained variance of a simple linear regression. The powers, shown in Table 2, ranged from 7 to 15. Then, for each day in the time series, the gridded wind speeds were multiplied by the correlations raised to the chosen power and summed across the domain. That is,

$$x = \sum_{j \in G} w_j^* z_j, \qquad (5)$$

where

$$w_j^* = w_j \Big/ \sum_{j \in G} w_j \quad \text{and} \quad w_j = [\text{corr}(y, z_j)]^p$$

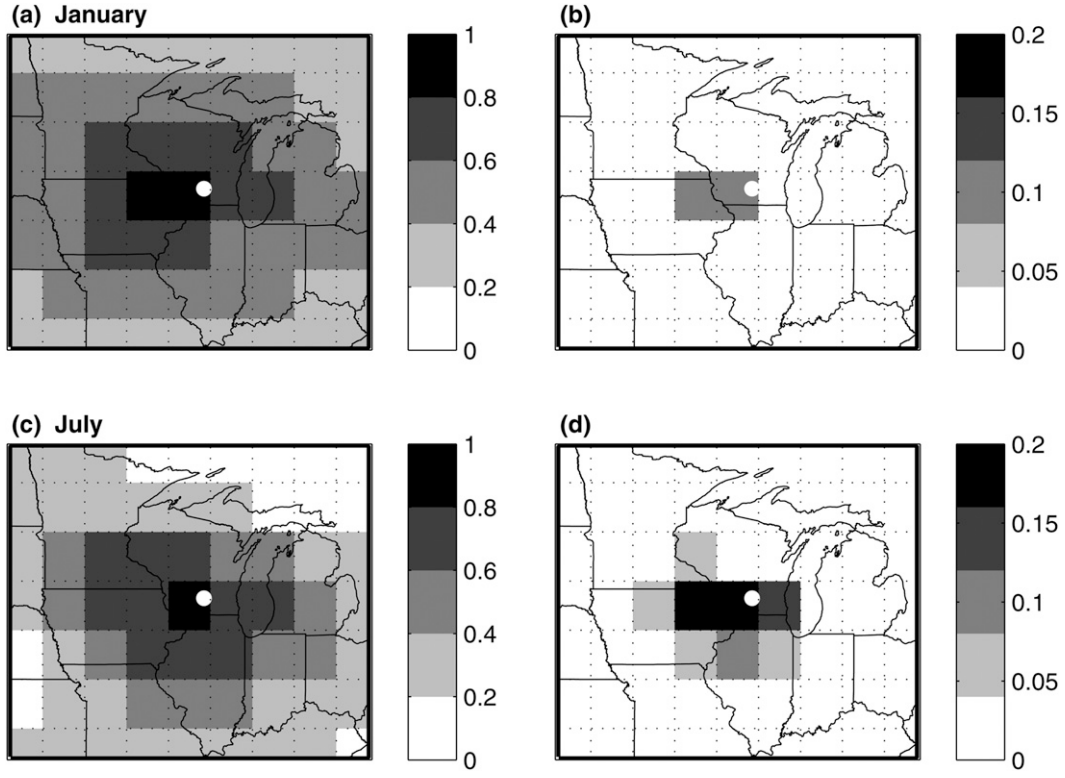

FIG. 8. Correlation between the local-scale wind speed at MSN (location shown with the dot) and each grid box of the reanalysis large-scale wind speed for (a) January and (c) July. (b),(d) As in (a),(c), but with the correlation map raised to the power p from Table 2.

and where, for a given station and month, x represents the large-scale wind, z_j represents the large-scale wind for grid box j in the gridded domain G, w_j represents the weight for that grid box and w_j^* is the weight after scaling so that

$$\sum_{j \in G} w_j^* = 1,$$

y is the local-scale wind, and p is the large, odd power. This procedure was repeated separately for every point location. Figures 8b and 8d show the correlation maps raised to the appropriate power p.

In Fig. 9, likelihood values are compared between the two methods for developing the predictor large-scale time series: interpolating to a point and using the correlation map as weights. The $-\log(L)$ values shown were summed across all sites, and the curves look very similar to those seen at individual stations. The correlation map–based predictor, with power p, produced consistently better likelihood values than those derived using the interpolation method. As further justification for raising the correlation map to a large, odd power, a similar curve is also plotted for the correlation-map predictor using a power of 1. Using the correlation map without a power produced poorer likelihood values than either of the previously mentioned choices. As a result, the correlation maps raised to the power p (Table 2) will be used to construct the large-scale time series for all following analyses.

A cross-validation technique was used to determine the number of predictors (2–6) for each site and month. To start, we defined a baseline estimate that used only the two constant parameters (γ_0 and D_0). This estimate was calculated as follows and represents the PDF of the local-scale wind if there is no influence from large-scale predictors. First, for a given site and month, two consecutive years of data were removed. A null model was fit with the two constant parameters on the remaining data. Using this fit, the $-\log(L)$ was calculated for the removed two years. This procedure was repeated for all nonoverlapping 2-yr periods, and the $-\log(L)$ values

TABLE 2. Powers chosen for the correlation-map predictor.

Jan	Feb	Mar	Apr	May	Jun	Jul	Aug	Sep	Oct	Nov	Dec
13	13	13	11	11	9	7	9	11	13	13	15

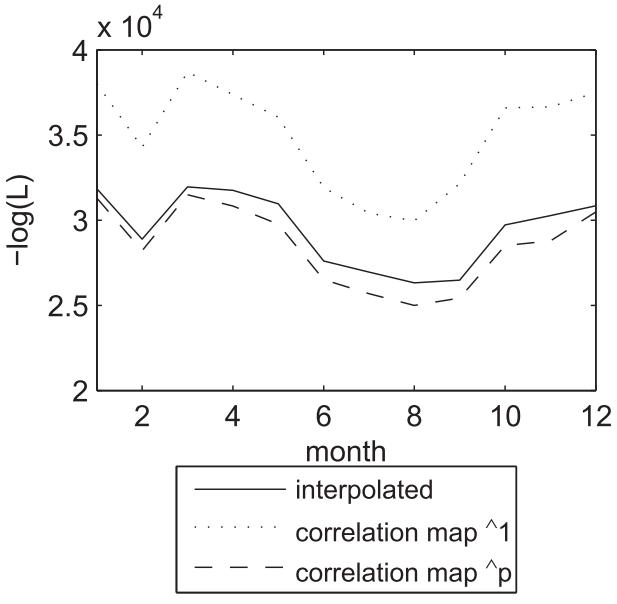

FIG. 9. Negative log-likelihood of the best-fit coefficients for each month using three different methods of forming the large-scale predictor time series: interpolating to the point, using the correlation map as weights, and raising the correlation-map weights to a power. Note that the optimal power p was determined for each month separately (see Table 2).

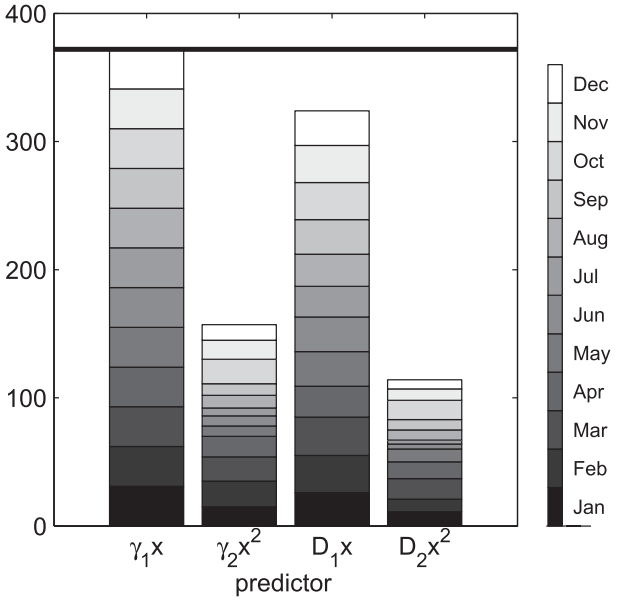

FIG. 10. Histogram depicting the number of cases (across all sites and all months) for which a given predictor was chosen. The maximum is 372. Months are represented by the shading.

were summed to get a baseline total for the whole period. This total is the null result against which we compared estimates that used daily-varying large-scale predictors.

Next, we computed conditional PDFs using some subset of the large-scale predictors. First, the less-two-years data were used to fit a model with three predictors. All remaining predictors were added individually, and the one producing the best likelihood values in the dataset was chosen. Using the three-predictor model fit with the longer dataset, the $-\log(L)$ was calculated for the 2-yr period. After repeating for all 2-yr periods, the $-\log(L)$ values were again summed. If this $-\log(L)$ total for three predictors was not better than that for two predictors, the process was terminated and the null two-predictor model was chosen; otherwise, a fourth predictor was tested. This process was repeated until the number of predictors was chosen or the full six-predictor model produced the best $-\log(L)$ totals. It is important to note that each independent period (each separate less-two-years period) calculated its own correlation map, chose its own power p, and chose its own link function coefficients α_μ and α_σ. Within each period, the p and α values were chosen across sites and months as mentioned in the previous discussions.

Next, using the number of predictors chosen through cross validation, a likelihood-based forward-selection method was employed to determine which of the six predictors would be used for the entire time series for each month. Figure 10 shows the number of cases for which a given predictor was chosen. Given that there are 31 sites and 12 months each, the maximum possible is 372. The linear predictor for the mean, $\gamma_1 x$, was chosen first for all cases, and $\gamma_2 x^2$ was chosen much less often. This result is consistent with Figs. 4a and 4c, where the plot of mean local-scale wind speed as a function of the mean large-scale wind speed showed a dominantly linear shape with only slight curvature at individual stations. The linear predictor for the standard deviation $D_1 x$ was also chosen for most cases. The choice of predictor $D_2 x^2$ was more seasonal, with this predictor being chosen for summer months much less often. A comparison of Figs. 4b and 4d shows January exhibiting a more parabolic shape than July, for which the curves are much flatter.

5. Results

In this section, we present an assessment of the downscaling model's performance. First, we summarize the use of the downscaling method and provide examples of the output. Next, we show validation of the method by comparing downscaled results with the observations.

For the downscaling procedure, a large-scale time series is created for each station's location (and for each month). This time series is inserted into the statistical

model as x. At this point, the model may be slightly different for each site and month, since the set of model predictors includes only those chosen through cross validation and forward selection. The output of the downscaling is a time series of mean values and a time series of standard deviation values, each of the same length as the input x. That is, the downscaling routine outputs a local-scale mean and standard deviation for each day of the input large-scale time series. By converting the mean and standard deviation values back into gamma distribution shape and scale parameters, a PDF is created for each day. The result is a daily-varying PDF that represents the range of possible local-scale daily wind speeds for each day, at each station, given the known large-scale wind speed for that day.

An example of the downscaling output is shown in Fig. 11. The downscaled PDFs (black curve) represent the quantified range of possible local-scale winds that could occur, given the known value for the large-scale wind for that day. We chose two days, one on which the large-scale wind speed was just under $2\,\mathrm{m\,s^{-1}}$ (Fig. 11a) and one on which the large-scale wind speed was closer to $8\,\mathrm{m\,s^{-1}}$ (Fig. 11b). The large-scale wind speed for each day is shown in dark gray, and the observed local-scale value is shown in light gray. The downscaling attempts to represent the range of possible local-scale wind speeds that could have occurred on each day, with the observed local-scale value representing only one possible value. The day characterized by a light large-scale wind has a shape parameter of $a = 6.5$ and a scale parameter of $b = 0.31$, whereas the day with a faster large-scale wind speed has a shape parameter of $a = 42.5$ and a scale parameter of $b = 0.17$. A comparison of the PDFs for these two days highlights that not only does each day have its own PDF, but the characteristics of that PDF are a direct function of the large-scale wind. Downscaling to a PDF maintains adequate variance at the local scale, in contrast to deterministic downscaling (i.e., estimating a single value for each day), which tends to underestimate the variance. In physical terms, this is because the large scale cannot contain all of the information for the local scale.

A downscaled realization can be generated by randomly selecting a value from each day's local-scale PDF. The result is a time series of possible local-scale values. This process can be repeated numerous times, because each realization is equally likely to occur. To put it more technically, a time series of independent, uniformly distributed random variables (RVs) is generated, of the same length as the observed time series. Then, a realization is generated by taking the inverse gamma distribution CDF of these uniformly distributed RVs, using the appropriate shape and scale parameters for each

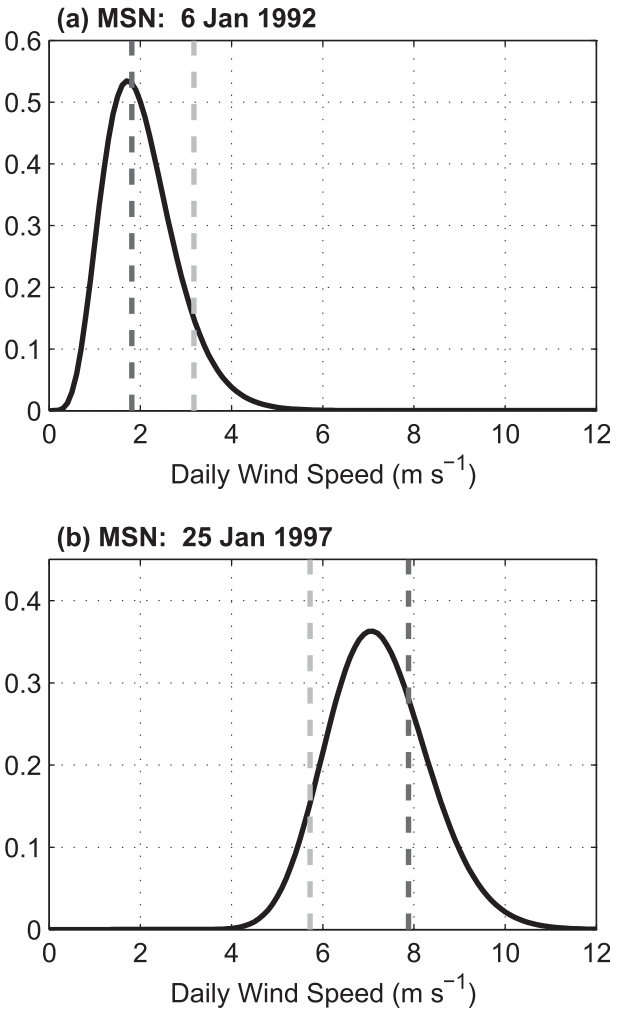

FIG. 11. Downscaled PDF (black curve) for (a) a day characterized by a small large-scale wind speed and (b) a day characterized by a large large-scale wind speed. The reanalysis large-scale value is shown in dark gray, and the observed local-scale value is shown in light gray.

day. Use of a time series of independent uniform RVs will only possess the autocorrelation that is residual from the large-scale wind speed, however. As is seen in Fig. 12a, this autocorrelation at lag 1 does not match that from observations; with few exceptions, the difference using 100 realizations at each site is statistically significant at the 99% level. Instead, a time series of uniform RVs with an appropriate autocorrelation can be used. We induce this autocorrelation by using a moving-average model with one parameter, written MA(1):

$$v_t = \epsilon_t + \theta\epsilon_{t-1},$$

$$U_t = \Phi\left(\frac{v_t}{\sqrt{1+\theta^2}}\right), \quad \text{and}$$

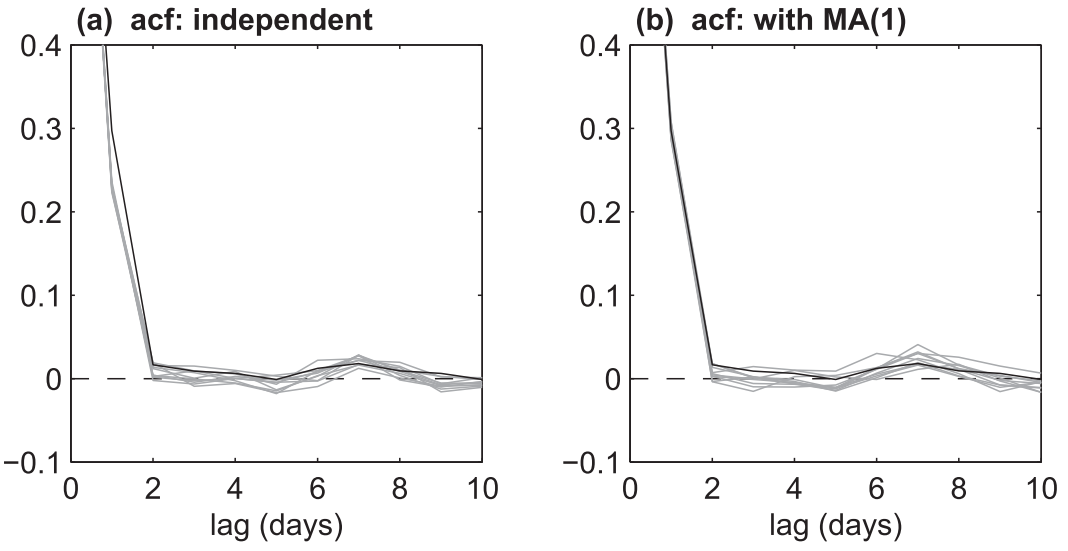

FIG. 12. Autocorrelation function for MSN (black line) and 10 downscaled realizations (gray lines) using (a) independent uniformly distributed random variables and (b) uniformly distributed random variables with the appropriate autocorrelation.

$$y_t^* = F^{-1}(U_t; a_t, b_t). \quad (6)$$

Here, v_t is created using an MA(1) model with coefficient θ, where the ϵ are independent and identically distributed as standard normal and t represents the current time step. Using the standard normal CDF Φ, v_t can be transformed into a standard uniform RV U_t. Then, the realization y_t^* is produced by taking the inverse gamma distribution CDF F^{-1} of U_t with the appropriate shape (a) and scale (b) parameter values for that day. The MA(1) coefficient θ was found by testing many potential values and choosing the one that minimized the difference between the lag-1 autocorrelations of the realization and observations. After repeating for 100 realizations, the average value for θ was determined; this θ was used in the equation for v_t above. The resulting autocorrelation functions of several realizations y^* are plotted in Fig. 12b. Now, the autocorrelations match well with what is seen in the observations and there is no significant difference (at the 99% level) between the lag-1 autocorrelation of the realizations and that from observations.

Figure 13 shows, in gray, 20 realization time series for 1 month. The black curve represents the actual observed local-scale wind speeds. Again, the goal of the downscaling routine is to represent the range of possible local-scale values for each day; it is not to reproduce the single observed value for each day. As such, we do not expect the realizations to exactly follow the observations, but we do expect the observed values to fall within the range of those realizations.

To assess the performance of the downscaling, quantile–quantile (QQ) plots of the predicted local-scale values versus observed local-scale values are shown in Fig. 14

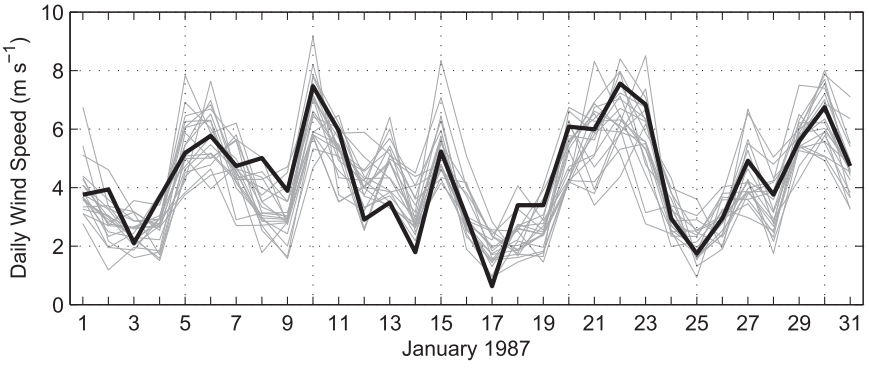

FIG. 13. Downscaled realizations of the local-scale daily wind speed for MSN in January 1987 (gray lines). The black line depicts the actual observed local-scale values.

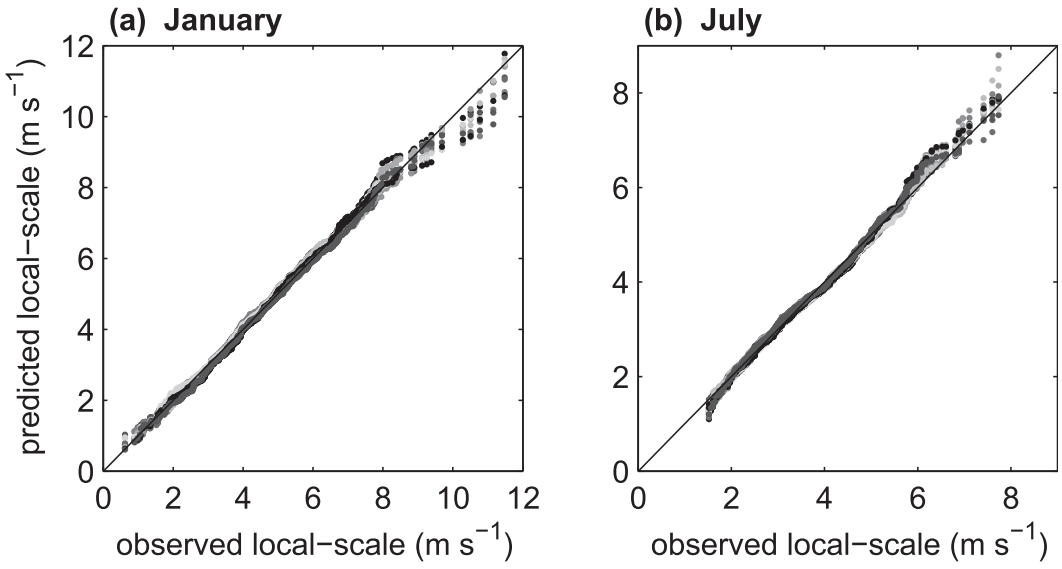

FIG. 14. QQ plot of the observed local-scale values against realizations of the local-scale values predicted by downscaling the reanalysis data for MSN in (a) January and (b) July. Ten different realizations are shown (represented by the different shades of gray). Points falling on the one-to-one line indicate that the two series come from the same distribution.

for MSN in January (Fig. 14a) and July (Fig. 14b). Each shade of gray represents a different realization. Ten different, equally likely realizations were sorted and plotted against the sorted time series of values observed at the site. Points on a QQ plot that fall on the one-to-one line indicate that the two datasets come from the same distribution and, in this case, suggest that the downscaling procedure accurately captured the distribution of the local-scale daily wind speed. Although shown for a single site, the results are consistent across the dataset.

To investigate the deviation from the QQ plot's one-to-one line at the upper-quantile (upper tail) points, the GEV distribution was fit to both the observed local-scale values and the predicted local-scale realizations. The purpose of this GEV analysis is to test how well our downscaling method captures the characteristics of the extremes. First, monthly time series were concatenated into seasonal time series [December–February (DJF), March–May, June–August (JJA), and September–November]. Next, each seasonal time series (for each site) was divided into blocks; we blocked the data by month and year. That is, each time series contained 27 yr of data for 3 months each year, resulting in 81 blocks. Then, the largest value from each of the blocks was extracted, and these block maxima were fit to a GEV distribution using an *L*-moments routine (Brodtkorb et al. 2000). GEV distributions are characterized by three types, based on the sign of the shape parameter: type I (Gumbel) has a shape parameter of zero, type II (Fréchet) has a positive shape parameter, and type III (Weibull) has a negative shape parameter.

We used a Monte Carlo approach to compare the GEV parameters. As above, seasonal block maxima were fit to the GEV distribution for 1000 downscaled realizations. Using the distribution of the shape parameters from these realizations, a 90% confidence interval was established. Figure 15 plots the observed shape parameter against the mean of the shape parameters from these 1000 realizations for DJF (Fig. 15a) and JJA (Fig. 15b). Points in black (gray) indicate that the observed shape parameter fell within (outside) the confidence interval established by the realizations. Most of the shape parameters identify with type I in the summer months, with a very slight shift toward type III in the winter months. Overall, most of the observed GEV shape parameters fall within the 90% confidence interval from the realizations. This agreement indicates that our downscaling method is accurately representing the characteristics of the daily wind speed extremes.

6. Discussion and conclusions

We use a probabilistic approach to statistically downscale daily wind variations, producing a daily-varying PDF that represents the range of possible local-scale wind speeds for each day, given the corresponding large-scale wind speed for that day. A probabilistic method maintains information on the variance and extremes in addition to the mean and also allows the autocorrelation

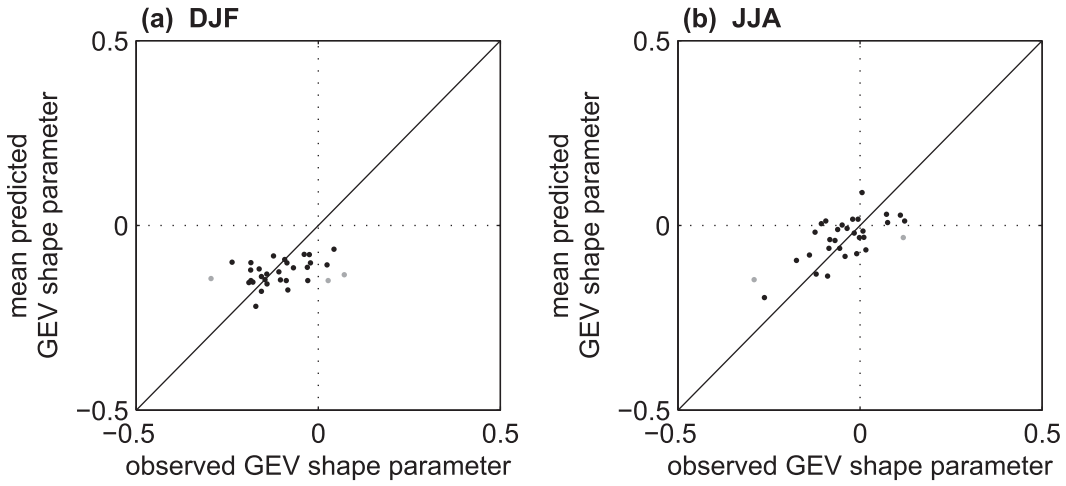

FIG. 15. Shape parameter of the GEV distribution for the observed local-scale winds against that for the predicted local-scale winds for (a) winter and (b) summer. A total of 1000 realizations (with appropriate autocorrelation) were used to construct 90% confidence intervals for the shape parameter; points in black (gray) indicate that the observed shape parameter falls within (outside) this confidence interval.

of downscaled realizations to be tuned to match that of observations. We used exploratory data analysis to investigate the structure of the relationship between local-scale and large-scale daily wind speed, finding that the mean, standard deviation, and gamma distribution shape parameter were all functions of the decile of the large-scale wind speed. As a result, we designed a statistical model to use large-scale wind speed to predict a gamma-distribution PDF of local-scale wind speed using a VGLM. Last, we implemented the statistical model and evaluated its performance. It was shown that the downscaling accurately captured the distribution of the local-scale wind speed. Producing a PDF maintains a reasonable variance for the local-scale wind and allows for the flexibility of the dataset to better fit with the needs of a variety of users. This method could be adapted for use with other variables or for a more specific investigation of extreme events.

Future work includes applying the downscaling method to a suite of debiased global climate models from phase 5 of the Coupled Model Intercomparison Project (CMIP5). By using multiple climate models, the set of downscaled PDFs can be compared to assess the spread of future responses. In addition, the spatial pattern of correlations (Fig. 8) shows the possibility for producing a gridded, downscaled dataset. We will accomplish this by interpolating the pointwise downscaled distribution parameters to a high-resolution grid, which will maintain the spatiotemporal variability. The downscaled PDFs can also be used for an in-depth analysis of extreme events, including an investigation of the large-scale conditions that produce local-scale extreme events and an estimation of changes in the probabilities of extreme events under future scenarios.

Acknowledgments. This work was funded by grants from the Wisconsin Focus on Energy Environmental and Economic Research and Development Program, the Upper Midwest and Great Lakes Landscape Conservation Cooperative, and the Nelson Institute Center for Climatic Research Climate, People, and the Environment Program. In addition, this work was partially supported by an American Meteorological Society Graduate Fellowship, sponsored by NOAA's Climate Program Office. We thank the editor, T. Sikora, for handling this manuscript and three anonymous reviewers for their insightful comments.

REFERENCES

Beckmann, B.-R., and T. Adri Buishand, 2002: Statistical downscaling relationships for precipitation in the Netherlands and north Germany. *Int. J. Climatol.,* **22,** 15–32.

Brodtkorb, P., P. Johannesson, G. Lindgren, I. Rychlik, J. Rydén, and E. Sjö, 2000: WAFO—A Matlab toolbox for the analysis of random waves and loads. *Proc. 10th Int. Offshore and Polar Engineering Conf.,* Vol. 3, Seattle, WA, International Society of Offshore and Polar Engineers, 343–350.

Bürger, G., T. Q. Murdock, T. Werner, S. R. Sobie, and J. Cannon, 2012: Downscaling extremes—An intercomparison of multiple statistical methods for present climate. *J. Climate,* **25,** 4366–4388.

Cheng, C. S., G. Li, Q. Li, and H. Auld, 2008: Statistical downscaling of hourly and daily climate scenarios for various meteorological variables in south-central Canada. *Theor. Appl. Climatol.,* **91,** 129–147.

——, ——, ——, ——, and C. Fu, 2012: Possible impacts of climate change on wind gusts under downscaled future climate conditions over Ontario, Canada. *J. Climate,* **25,** 3390–3408.

Coleman, T. F., and Y. Li, 1996: An interior trust region approach for nonlinear minimization subject to bounds. *SIAM J. Optim.,* **6,** 418–445.

de Rooy, W. C., and K. Kok, 2004: A combined physical–statistical approach for the downscaling of model wind speed. *Wea. Forecasting,* **19,** 485–495.

Engen-Skaugen, T., 2007: Refinement of dynamically downscaled precipitation and temperature scenarios. *Climatic Change,* **84,** 365–382.

Fealy, R., and J. Sweeney, 2007: Statistical downscaling of precipitation for a selection of sites in Ireland employing a generalised linear modelling approach. *Int. J. Climatol.,* **27,** 2083–2094.

Frías, M. D., E. Zorita, J. Fernández, and C. Rodríguez-Puebla, 2006: Testing statistical downscaling methods in simulated climates. *Geophys. Res. Lett.,* **33,** L19807, doi:10.1029/2006GL027453.

Fuentes, U., and D. Heimann, 2000: An improved statistical–dynamical downscaling scheme and its application to the Alpine precipitation climatology. *Theor. Appl. Climatol.,* **135,** 119–135.

Giorgi, F., 2006: Regional climate modeling: Status and perspectives. *J. Phys. IV,* **139,** 101–118.

Goubanova, K., V. Echevin, B. Dewitte, F. Codron, K. Takahashi, P. Terray, and M. Vrac, 2010: Statistical downscaling of sea-surface wind over the Peru–Chile upwelling region: Diagnosing the impact of climate change from the IPSL-CM4 model. *Climate Dyn.,* **36,** 1365–1378.

Hastie, T., and R. Tibshirani, 1986: Generalized additive models. *Stat. Sci.,* **1,** 297–318.

Horvath, K., D. Koracin, R. Vellore, J. Jiang, and R. Belu, 2012: Sub-kilometer dynamical downscaling of near-surface winds in complex terrain using WRF and MM5 mesoscale models. *J. Geophys. Res.,* **117,** D11111, doi:10.1029/2012JD017432.

Kalnay, E., and Coauthors, 1996: The NCEP/NCAR 40-Year Reanalysis Project. *Bull. Amer. Meteor. Soc.,* **77,** 437–471.

Lagarias, J. C., J. a. Reeds, M. H. Wright, and P. E. Wright, 1998: Convergence properties of the Nelder–Mead simplex method in low dimensions. *SIAM J. Optim.,* **9,** 112–147.

Leander, R., and T. A. Buishand, 2007: Resampling of regional climate model output for the simulation of extreme river flows. *J. Hydrol.,* **332,** 487–496.

Maraun, D., H. W. Rust, and T. J. Osborn, 2010a: Synoptic airflow and UK daily precipitation extremes. *Extremes,* **13,** 133–153.

——, and Coauthors, 2010b: Precipitation downscaling under climate change: Recent developments to bridge the gap between dynamical models and the end user. *Rev. Geophys.,* **48,** RG3003, doi: 10.1029/2009RG000314.

Martinez, Y., W. Yu, and H. Lin, 2013: A new statistical–dynamical downscaling procedure based on EOF analysis for regional time series generation. *J. Appl. Meteor. Climatol.,* **52,** 935–952.

McCullagh, P., and J. Nelder, 1989: *Generalized Linear Models*. 2d ed. CRC Press, 511 pp.

Mengelkamp, H., H. Kapitza, and U. Pflueger, 1997: Statistical-dynamical downscaling of wind climatologies. *J. Wind Eng. Ind. Aerodyn.,* **67–68,** 449–457.

Michelangeli, P.-A., M. Vrac, and H. Loukos, 2009: Probabilistic downscaling approaches: Application to wind cumulative distribution functions. *Geophys. Res. Lett.,* **36,** L11708, doi:10.1029/2009GL038401.

Monahan, A. H., 2012: Can we see the wind? Statistical downscaling of historical sea surface winds in the subarctic northeast Pacific. *J. Climate,* **25,** 1511–1528.

Najac, J., C. Lac, and L. Terray, 2011: Impact of climate change on surface winds in France using a statistical-dynamical downscaling method with mesoscale modelling. *Int. J. Climatol.,* **31,** 415–430.

Oh, J.-H., T. Kim, M.-K. Kim, S.-H. Lee, S.-K. Min, and W.-T. Kwon, 2004: Regional climate simulation for Korea using dynamic downscaling and statistical adjustment. *J. Meteor. Soc. Japan,* **82,** 1629–1643.

Panofsky, H. A., and G. W. Brier, 1958: *Some Applications of Statistics to Meteorology*. Mineral Industries Continuing Education, College of Mineral Industries, The Pennsylvania State University, 224 pp.

Pryor, S. C., J. Schoof, and R. Barthelmie, 2005: Empirical downscaling of wind speed probability distributions. *J. Geophys. Res.,* **110,** doi:10.1029/2005JD005899.

Salameh, T., P. Drobinski, M. Vrac, and P. Naveau, 2009: Statistical downscaling of near-surface wind over complex terrain in southern France. *Meteor. Atmos. Phys.,* **103,** 253–265.

Schmidli, J., C. M. Goodess, C. Frei, M. R. Haylock, Y. Hundecha, J. Ribalaygua, and T. Schmith, 2007: Statistical and dynamical downscaling of precipitation: An evaluation and comparison of scenarios for the European Alps. *J. Geophys. Res.,* **112,** D04105, doi:10.1029/2005JD007026.

Schmith, T., 2008: Stationarity of regression relationships: Application to empirical downscaling. *J. Climate,* **21,** 4529–4537.

van der Kamp, D., C. L. Curry, and A. H. Monahan, 2012: Statistical downscaling of historical monthly mean winds over a coastal region of complex terrain. II. Predicting wind components. *Climate Dyn.,* **38,** 1301–1311.

Vrac, M., M. Stein, and K. Hayhoe, 2007: Statistical downscaling of precipitation through nonhomogeneous stochastic weather typing. *Climate Res.,* **34,** 169–184.

Wood, A. W., 2002: Long-range experimental hydrologic forecasting for the eastern United States. *J. Geophys. Res.,* **107,** 4429, doi:10.1029/2001JD000659.

Yan, Z., S. Bate, R. Chandler, V. Isham, and H. Wheater, 2002: An analysis of daily maximum wind speed in northwestern Europe using generalized linear models. *J. Climate,* **15,** 2073–2088.

Yang, C., R. E. Chandler, V. S. Isham, and H. S. Wheater, 2005: Spatial–temporal rainfall simulation using generalized linear models. *Water Resour. Res.,* **41,** W11415, doi:10.1029/2004WR003739.

Yee, T. W., and A. G. Stephenson, 2007: Vector generalized linear and additive extreme value models. *Extremes,* **10,** 1–19.